Electronic Supplementary Information

Tailoring the nanostructures of electrochemical actuators for fast response and large deformation

Liang Ji[†], Yiwen Yu[†], Qian Deng[†,‡,*], Shengping Shen[†,§,*]

[†]State Key Laboratory for Strength and Vibration of Mechanical Structures, School of Aerospace Engineering, Xi'an Jiaotong University, Xi'an 710049, China

[‡]Department of Engineering Mechanics, School of Aerospace Engineering, Xi'an Jiaotong University, Xi'an 710049, China

[§]Department of Aeronautics & Astronautics Engineering, School of Aerospace Engineering, Xi'an Jiaotong University, Xi'an 710049, China

*Corresponding authors: sshen@mail.xjtu.edu.cn (S.S.); tonydqian@mail.xjtu.edu.cn (Q.D.)

Supporting Information Outline:

Section S1. Calculations of actuation

The actuation mechanism and structure of the bilayered EA are schematically shown in Fig. S1. Fig. S1a indicates that the EA is considered as a composite bilayered cantilever beam. When actuator works as the cathode, the hydrogen ions freely moved in electrolyte begin migrating towards the actuator. After migrating through SEI, the intercalated hydrogen ions interact with MoS_2 on the surface, which forms H_xMoS_2 structure. The remaining hydrogen ions then keep migrating into deeper region of MoS_2 and the same interaction is repeated until the x reaches its maximum. When actuator works as the anode, whole interaction mentioned above will reverse. H_xMoS_2 will decompose and the hydrogen ions will de-intercalate from actuator. The reaction will be carried out once the potential reaches about -0.3V. Here, x is in the range of $0.012<x<0.84.$[1]

$$xH^+ + xe^- + MoS_2 \rightleftharpoons H_xMoS_2 \text{ (\~-0.3V VS SCE)} \tag{S1}$$
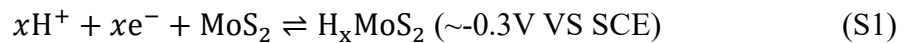
Theoretically, the actuator film is assumed to be perfectly bonded to the substrate both in initial and intercalated states. The competition and interaction between the substrate and the actuator film lead to the bending effect in Fig. S1b.
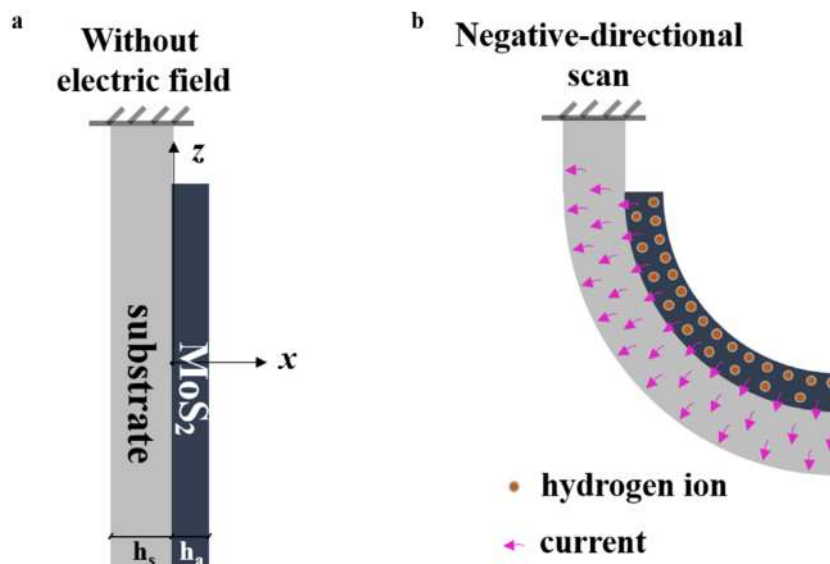

Fig. S1 Configurations of (a) initial state and (b) bent state. The subscripts "s" and "a" in (a) represent the substrate and the actuator film, respectively.

Bending, which is the crucial factor of actuator, benefits from the electrochemical potential μ:

$$\mu = \mu_0 + RT\ln c - \Omega\sigma_h - \left(\frac{\lambda \int_0^t c\, dt}{\xi t}\right)\sigma_h + zF\varphi \tag{S2}$$

where the hydrostatic pressure $\sigma_h = \frac{1}{3}(\sigma_{xx} + \sigma_{yy} + \sigma_{zz})$ (N·m^{-2}), μ_0 is the invariant reference potential (J·mol^{-1}), R and T are gas constant (J·K^{-1}·mol^{-1}) and temperature (K), respectively. c is the concentration of solute (mol·m^{-3}), the second term after equal sign represents the potential contribution of configurational entropy. Ω is the partial molar volume of intercalated ion (m^3·mol^{-1}), λ is the chemical reaction factor (m$^{5/2}$·mol$^{-5/2}$·s^{-1}), ξ is the chemical reaction rate (mol$^{-1/2}$·m$^{-7/2}$·s^{-1}). Both the third and the fourth terms embody the influence of stress on potential. z is the effective charge (a.u.), F is the Faraday constant (C·mol^{-1}), φ is the electric potential (V), the fifth term represents the potential contribution of electric field.

Ions diffusion satisfies the law of mass conservation:

$$\frac{\partial c}{\partial t} = \nabla(Mc\nabla\mu) \tag{S3}$$

where M is the ion mobility in host material (m^2·mol·J^{-1}·s^{-1}).

Substituting Equation (S2) into (S3) gives:

$$\frac{\partial c}{\partial t} = D\frac{\partial}{\partial x}\left\{\frac{\partial c}{\partial x} - \frac{c}{RT}\frac{\partial \Omega\sigma_h}{\partial x} - \frac{c}{RT}\frac{\partial\left(\frac{\lambda \int_0^t c\, dt}{\xi t}\right)\sigma_h}{\partial x} + \frac{c}{RT}\frac{\partial zF\varphi}{\partial x}\right\} \tag{S4}$$

where $D = MRT$ is the ion diffusivity (m^2·s^{-1}). Without the consideration of diffusion, chemical reaction and electric field, Equation (S4) is reduced to the classic diffusion formula:

$$\frac{\partial c}{\partial t} = D\frac{\partial}{\partial x}\left(\frac{\partial c}{\partial x}\right) \tag{S5}$$

The initial concentration of solute in host material is assumed to be zero:

$$c(x, 0) = 0 \tag{S6}$$

The interface ($x = 0$) between the substrate and the actuator film acts as the dividing line between the ions-existent region (MoS$_2$) and ion-inexistent region (metal foil), ion flux is considered to have no variation along the thickness direction at this interface. Therefore, the boundary condition is given by :

$$D \frac{\partial c(0, t)}{\partial x} = 0 \tag{S7}$$

Since cyclic voltammetry measurement is carried out in this work, the solute concentration at the surface ($x = h_a$) of EA is therefore controlled by the electric potential applied on the working electrode. Theoretically, the charge transfer at SEI has to be at the equilibrium state for a reversible electrochemical system. The electron transfer is considered to be rapidly enough to satisfy the Nernst equilibrium. Therefore, the boundary condition at the surface of actuator film is expressed as:

$$c(h_a, t) = c_0 \left\{ 1 - exp \left[\frac{(\varphi - \varphi_0)nF}{RT} \right] \right\} \tag{S8}$$

where φ_0 is the formal potential of system, c_0 is considered as the source concentration of intercalated solute in electrolyte. Since both oxidation and reduction reactions occur during electrochemical measurements. c_0 could also be converted into the concentration of oxidized or reduced species in solution.

In order to study the ion diffusion along thickness direction (x-direction), the actuator film is considered to be a large plate in y- and z-directions. Based on the classical Euler–Bernoulli beam theory, plane section remains plane after deformation, this hypothesis means that shear deformations and shear stresses are equal to zero. Moreover, stress along x-direction (thickness direction) is zero. As a first approximation, y- and z-directions in large plate are considered to have the same concentration distribution of intercalated ions. Thus, we assume that the stresses

along y- and z-directions are equal, $i.e.$, $\sigma_{zz} = \sigma_{yy}$. Actuation force, which is the other important parameter of EAs, mainly consists of the following parts:

$$\sigma_a = \sigma_{yy} = \sigma_{zz}$$
$$= \sigma_{\text{in-plane}} - \sigma_{\text{diffusion}} - \sigma_{\text{reaction}} - \sigma_{\text{flexoelectricity}} - \sigma_{\text{piezoelectricity}}$$

(S9)

The in-plane stress is a function of thickness x and curvature κ:

$$\sigma_{\text{in-plane}} = Y_a(\varepsilon_{x=0} + \kappa x)$$

(S10)

where Y_a is the Young's modulus of actuator film (N·m^{-2}), $\varepsilon_{x=0}$ is the strain at the interface between the substrate and the actuator film.

The second term of Equation (S9) represents the diffusion-induced stress:

$$\sigma_{\text{diffusion}} = Y_a c \Omega$$

(S11)

Both theoretical and experimental studies[2,3] have demonstrated that the chemical reaction could also cause the volume strain by effecting the formation of reaction compound. Thus, the third term is used to describe the chemical reaction-induced stress:

$$\sigma_{\text{reaction}} = Y_a \lambda \int_0^t c \, dt$$

(S12)

MoS$_2$ has three material states, namely, 1T-phase, 2H-phase and 3R-phase. 1T- and 3R-MoS$_2$ have a metastable crystal structure while 2H-MoS$_2$ has a stable crystal structure. Moreover, 1T- and 2H-MoS$_2$ have the metallic and semiconducting properties, respectively. It should be pointed out that the electric field within metallic MoS$_2$ could be considered uniform. That means the electric field has little influence on ions-migration.[4] In this case, diffusion and chemical reaction would play a more important role. However, once 2H-MoS$_2$ is fabricated, the converse flexoelectric and piezoelectric effects will be prominent:[5-7]

$$\sigma_{\text{flexoelectricity}} = Y_a f \frac{\partial E}{\partial x} = Y_a f \frac{\partial^2 \varphi}{\partial x^2}$$

(S13)

$$\sigma_{\text{piezoelectricity}} = Y_a dE = Y_a d \frac{\partial \varphi}{\partial x}$$

(S14)

where f is the converse flexoelectric coefficient (C·m^{-1}), f_{1133} links to the strain gradient along the x-direction of the film. E is the electric field strength (V·m^{-1}), d is the converse piezoelectric coefficient (m·V^{-1}), d_{111} and d_{133} link to the strain along the x-direction and z-direction, respectively.

Substituting Equations (S10)-(S14) into (S9) gives:

$$\sigma_a = Y_a(\varepsilon_{x=0} + \kappa x) - \frac{Y_a}{3}\left(c\Omega + \lambda\int_0^t c\, dt + f\frac{\partial^2\varphi}{\partial x^2} + d\frac{\partial\varphi}{\partial x}\right) \tag{S15}$$

Since the substrate is perfectly bonded to the actuator film, the stress in substrate is solely influenced by the in-plane strain:

$$\sigma_s = Y_s(\varepsilon_{x=0} + \kappa x) \tag{S16}$$

where Y_s is the Young's modulus of substrate.

There are no mechanical loads applied on the surfaces of substrate and actuator film, the mechanical equilibrium conditions are therefore expressed as:

$$\int_{-h_s}^{h_a} \sigma_a\, dx = 0 \tag{S17}$$

$$\int_{-h_s}^{h_a} \sigma_a x\, dx = 0 \tag{S18}$$

Respectively substituting Equation (S15) into (S17) and (S18) gives:

$$\begin{aligned}\varepsilon_{x=0}\int_{-h_s}^{h_a} Y_a\, dx &+ \kappa\int_{-h_s}^{h_a} Y_a x\, dx \\ &= \frac{Y_a}{3}\int_0^{h_a}\left(c\Omega + \lambda\int_0^t c\, dt + f\frac{\partial^2\varphi}{\partial x^2} + d\frac{\partial\varphi}{\partial x}\right) dx\end{aligned} \tag{S19}$$

$$\begin{aligned}\varepsilon_{x=0}\int_{-h_s}^{h_a} Y_a x\, dx &+ \kappa\int_{-h_s}^{h_a} Y_a x^2\, dx \\ &= \frac{Y_a}{3}\int_0^{h_a}\left(c\Omega + \lambda\int_0^t c\, dt + f\frac{\partial^2\varphi}{\partial x^2} + d\frac{\partial\varphi}{\partial x}\right) x\, dx\end{aligned} \tag{S20}$$

The curvature is obtained by:

$$\kappa = \frac{BC - AF}{B^2 - AE} \tag{S21}$$

where

$$A = \int_{-h_s}^{h_a} Y_a \, dx \qquad B = \int_{-h_s}^{h_a} Y_a \, x \, dx \qquad E = \int_{-h_s}^{h_a} Y_a \, x^2 \, dx \tag{S22a-e}$$

$$C = \frac{Y_a}{3} \int_0^{h_a} \left(c\Omega + \lambda \int_0^t c \, dt + f \frac{\partial^2 \varphi}{\partial x^2} + d \frac{\partial \varphi}{\partial x} \right)$$

$$F = \frac{Y_a}{3} \int_0^{h_a} \left(c\Omega + \lambda \int_0^t c \, dt + f \frac{\partial^2 \varphi}{\partial x^2} + d \frac{\partial \varphi}{\partial x} \right) x \, dx$$

The gravimetric capacitance C of the working electrode is calculated by:

$$C = \frac{\int I \, dV}{2 \cdot SR \cdot \Delta V \cdot m} \tag{S23}$$

where V and I are the applied voltage and current, respectively. SR is the scan rate, ΔV is the voltage range, m is the weight of MoS_2 film.

Energy density W is one of the important parameters to judge the actuator performance:[8]

$$W = \frac{1}{2} Y \varepsilon^2 \tag{S24}$$

where $\varepsilon = \Delta\kappa \cdot x$ is the bending-induced strain, $\Delta\kappa$ is the curvature change from the initial state to the calculated state (i.e., actuated state at some time), while x represents the distance from the calculated point to the neutral axis of actuator. Based on the classical Euler–Bernoulli beam theory, x is a constant value for a certain point both at initial state and actuated state. The Young's modulus of the composite bilayered actuator Y is given by:

$$Y = Y_s \cdot \frac{h_s}{h_s + h_a} + Y_a \cdot \frac{h_a}{h_s + h_a} \tag{S25}$$

Section S2. Comparison between NPs-aggregated nanoporous structure and layer-stacked structure

As mentioned in the introduction, the nanostructures of EAs have experienced huge changes during the last decade. In this section, we mainly discuss the reason why there is such a

significant difference among the response rates of differently nanostructured EAs. The NPs-aggregated nanoporous structure and the nanosheets (NSs)-stacked layered structure are studied comparatively.

Based on the SEM images and granularmetric analysis (Section S4; Extended data Fig. 1d,e[9]), NPs-aggregated nanoporous structure and NSs-stacked layered structure could be approximately considered to be consisted of nano-circles (diameters vary from 85 to 475nm) and nano-flakes with different size (85-475nm) and thickness (10-20nm) in the modeling. The simulated models of NPs-aggregated nanoporous and NSs-stacked layered structures are depicted in Fig. S2. Porosities of NPs-structure and NSs-structure are 0.22 and 0.19, respectively. It should be pointed out that ion intercalation is actually a complex process, which involves ion movement in electrolyte, migration through SEI and intercalation in host material. Once the nanoporous film is immersed into electrolyte, pores will be filled with liquid electrolyte and act as the source of intercalated ions. That means porosity mainly affects the chemical activities in liquid phase and can hardly affect the ion diffusion within the solid host materials.

NPs-aggregated computational model was generated based on the theory for the random generation of porous electrode.[10] The generation process, which is linked with the secondary development of COMSOL-Multiphysics, consist of the following steps: i) Initialize and define the total number of the differently sized circles in a rectangular domain; ii) Initialize a set of double precision function, which could be used to fix the x/y position and radius of each particle and define the maximum and minimum value of radius; iii) Define the x/y coordinates with calling stochastic method and scaling output method. It could ensure the x/y position of NPs are located within the outer limit of the model; iv) Check the location and size of the NPs to avoid them out of the rectangular domain. v) Then, the main structure of porous electrode is established. Every time we use this method, a new distribution would be obtained. Solute diffusion within the host material is assumed to be isotropic. The intercalation process of ion

flux is governed by Nernst equilibrium. It is worthwhile to mention that diffusion mechanisms are drastically different in these two models. Actually, both of the solid-liquid diffusion and the solid-solid diffusion will occur during the charging process. However, the solid-solid diffusion has a slower rate and a lower efficiency than the solid-liquid diffusion.[11] Therefore, the solid-solid contact could be approximately considered as a blocking effect for ion diffusion. Ions mostly intercalate along the radial direction of NPs, however, they have to migrate along the longest length direction of NSs because the stacking of NSs causes a large-area contact and blocks the intercalation along the thickness direction (shortest way) of NS. As a result, the lengths of diffusion paths, which are drastically different for these two structures, significantly influence the response rates of these two EAs. In order to quantitatively analyze the length effects, the average lengths of these two structures are obtained by calculating the average distances from the SEI to the centroid of each NS and NP. The average diffusion paths in NPs-model and NSs-model are 74.954nm and 135.513nm, respectively. Since diffusivity coefficient of the intercalated hydrogen ions in MoS_2 has not been explored in existing references, the diffusivity coefficient of hydrogen ions within graphene oxide is used in this simulation ($D = 6.2 \times 10^{-6} \mathrm{m}^2 \cdot s^{-1}$).[12] It should be pointed out that although this diffusivity coefficient has a deviation from the real value, both NPs-model and NSs-model use the same material constants in simulation. That means the comparison between the diffusion processes within these two structures are still effective.
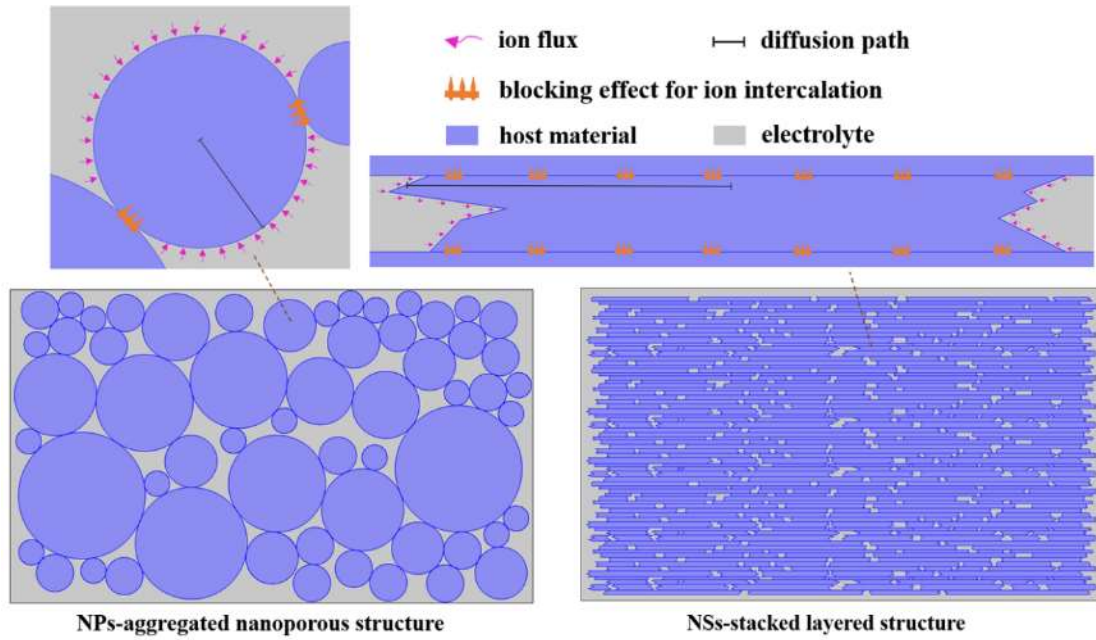
Fig. S2 Simulated models of NPs-aggregated nanoporous structure and NSs-stacked layered structure.

Fig. S3 shows the comparison between the average intercalation rates of NPs-structure and NSs-structure. The values of intercalation state 0 and 1 represent the un-intercalated state and fully intercalated state, respectively. At the initial stage of electrochemical measurement, the drastically increased intercalation state is caused by the huge concentration gradient of intercalated ions between the electrolyte and the inner region of host materials. Then it gradually flattens because the decrescent concentration gradient cannot provide enough driving force for ion intercalation. In-situ observed curvature under the experimental conditions of 10mV/s, $\pm 0.7V$ and electrolyte PH value of 0.99 is also shown in Fig. S3, it can be seen clearly that bending curvature shows the similar variation trend as the intercalation state. This is due to that bending effect of EA is caused by the intercalation-induced volume change of host material. k_1 and k_2 represent the response rates of NSs-structure and NPs-structure, respectively. The ratio $\frac{k_1}{k_2} = 0.555$ is approximately equal to the derivative of the ratio between diffusion lengths of NSs- and NPs-structures ($\frac{1}{\left(\frac{133.513nm}{74.954nm}\right)} = 0.561$). Therefore, it could be concluded that the response rate of EA is determined by the length of ions-diffusion path in nano-granules. NPs-aggregated nanoporous structure provides the shortest path for ions diffusion, which ensures a

10

fast response rate of this EA. Therefore, granular size and shape of nanomaterials, which are crucial to improve the actuator performance, will attract more attentions in our future research.
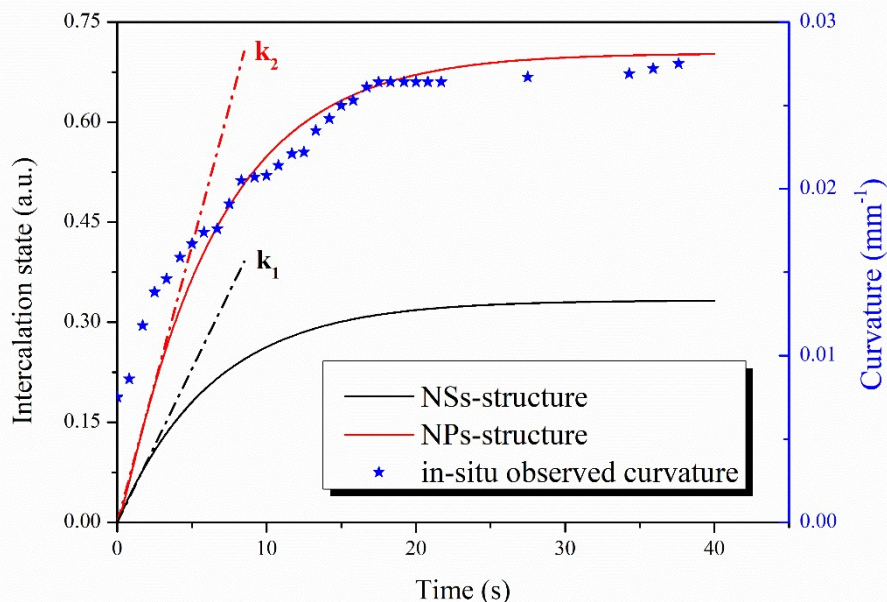

Fig. S3 Comparison between the average intercalation rates of NPs-aggregated nanoporous structure and NSs-stacked layered structure.

Section S3. Relation between Raman shift and thickness of film

The shift difference between A_{1g} and E^1_{2g} in Raman spectrum could be used to characterize the thickness of the grown film, for example, 18cm^{-1} for monolayer,[13] 22.5cm^{-1} for bilayer,[14] 23.8cm^{-1} for trilayer[14] and greater than 25cm^{-1} for bulk MoS_2.[14] In this work, the value is equal to 26.4cm^{-1}, which corresponds to the 4μm MoS_2 film. This thickness was also verified by thickness measurement in characterization.

Section S4. Size polydispersity of the NPs

Fig. 3a has demonstrated that the grown MoS_2 film consists of numerous spherical NPs. A TEM observation was performed to further investigate the interior characters of the thick film. Before the observation, we mechanically peeled off the MoS_2 film with the tape and then pressed into the ethanol solution to form the suspension, which was then dropped on the carbon substrate and dried for twenty minutes. It should be pointed out that the exfoliation of MoS_2 in

first few times should not be used. It can be seen clearly in Fig. S4a that MoS_2 at interior zone also appears as the spherical NPs with different sizes. Based on a more than 2500-NPs statistical analysis of SEM images, granularmetric analysis was carried out and the result is shown in Fig. S4b, sizes of the NPs vary from 100nm to 500nm. Moreover, majority of the NPs are found to have a diameter of 100-120nm, average size of the NPs is 220.95nm with a standard deviation of 111.06nm.
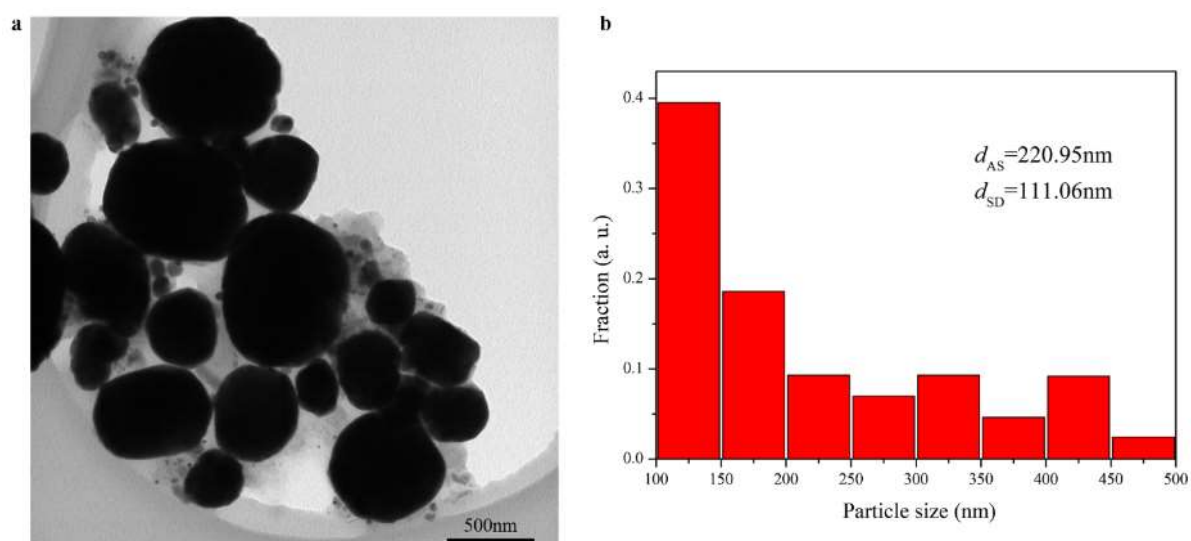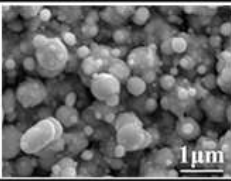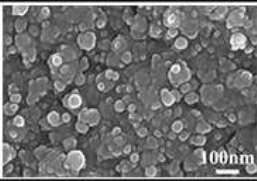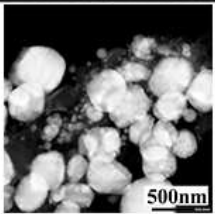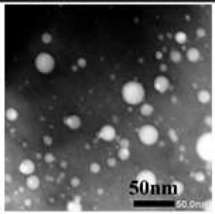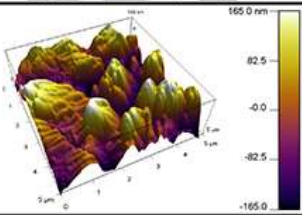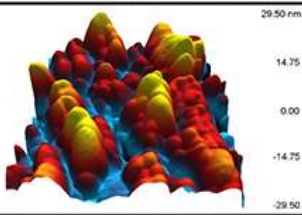

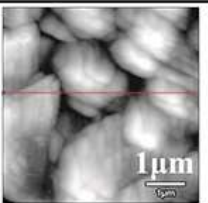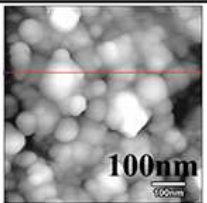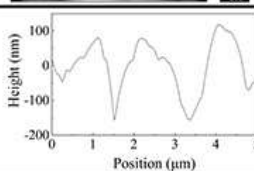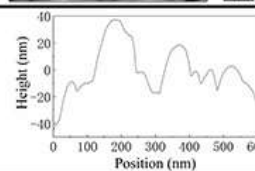**Fig. S4** (a) TEM image of the mechanically exfoliated MoS_2 NPs. (b) Granularmetric analysis of the NPs, the subscripts "AS" and "SD" represent the average size and standard deviation, respectively.

Section S5. Influence of PLD parameters on nanostructures

PLD Parameters	Laser energy: 40mJ/mm² Pressure: 4×10⁻⁷Torr	Laser energy: 75mJ/mm² Pressure: 5×10⁻⁸Torr
SEM		
TEM		
AFM 3D plot		
AFM topology		
Roughness along the red line of AFM topology		

Fig. S5 Influence of laser energy and vacuum degree on nanostructures of MoS_2.

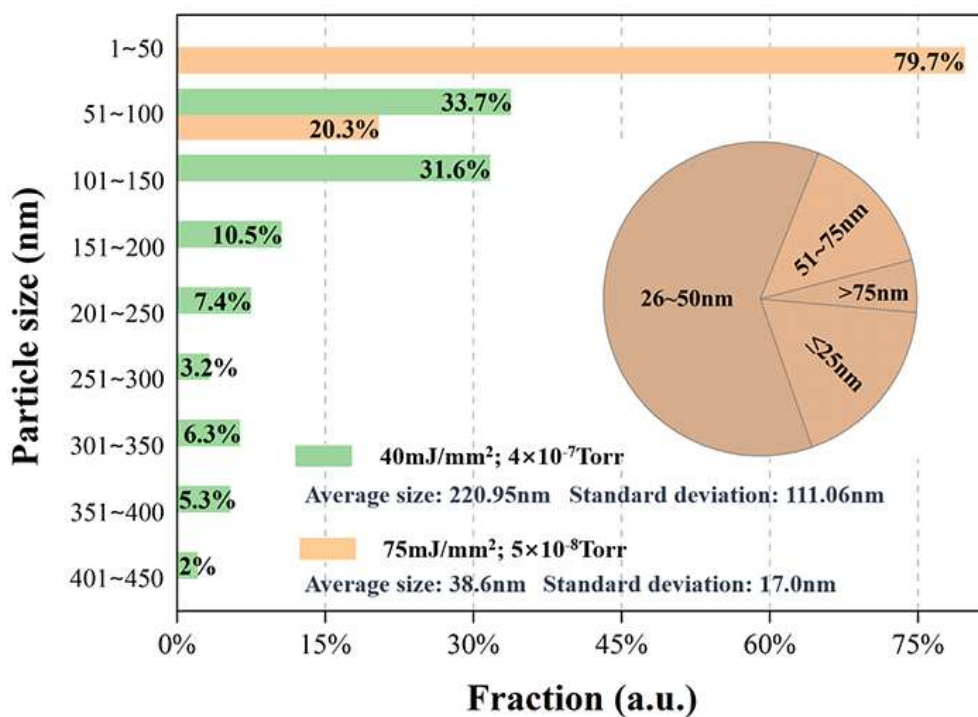## Section S6. Relation between specific capacitance and potential

Fig. S6 illustrates the relation between the specific capacitance and the applied potential at different scan rates. An approximately linear relation is captured especially at relatively high scan rate (0.02-0.07V/s). While under low-rate scan (0.005-0.01V/s), an increase of the specific capacitance is shown when the applied potential is higher than 0.5V. This is due to that the electrochemical reaction can be adequately carried out in this material system under low-rate scan, a higher potential provides a larger driving force to arrange the charges within host material.
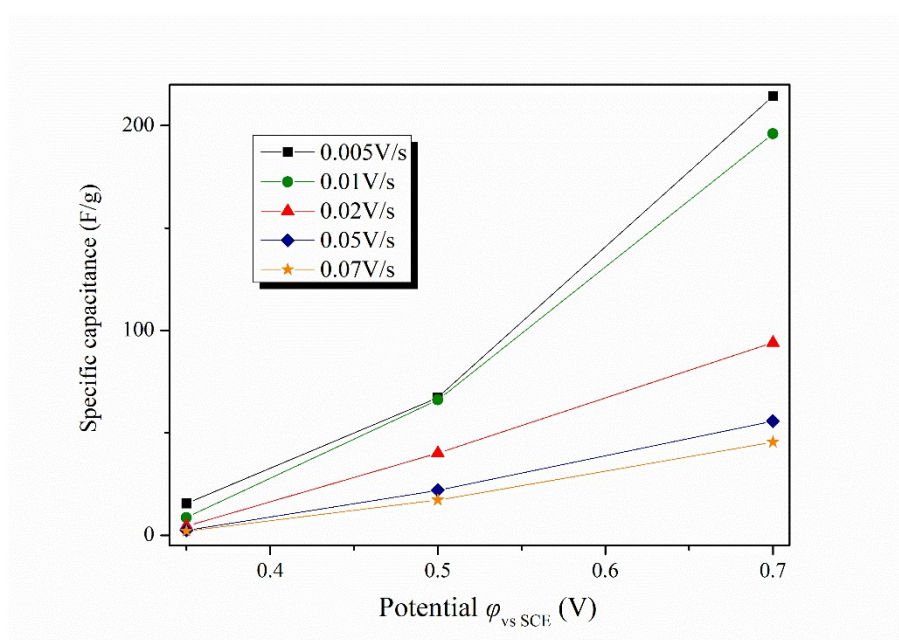
Fig. S6 Specific capacitance versus the applied potential at different scan rates.

Section S7. Comparison among actuators

Tab. S1 Characteristics of different kinds of actuators.

Actuation principle	Working voltage (V)	Power consumption (mW)	Reference
Electrostatic	100-200	<1	15
Thermopneumatic	~5	~2000	16
Electromagnetic	20-50	$1\text{-}2.5\times10^{6}$	17
Piezoelectric	40-100	<5	18
Electrothermal	~4	~1000	19
Electrochemical	0.3-4	1.5-15	

14

Tab. S2 Comparison among existing EAs.

Type	Curvature (mm^{-1})	Response rate $(mm^{-1} \cdot s^{-1})$	Amplitude of working voltage (V)	Voltage-dependent curvature $(mm^{-1} \cdot V^{-1})$	Voltage-dependent response rate $(mm^{-1} \cdot s^{-1} \cdot V^{-1})$	Reference
graphene	0.067	6.7×10^{-3}	1.2	0.0558	5.58×10^{-3}	20
RGO-MWCNT	0.061	0.0305	2.5	0.0244	0.0122	21
RGO-Ag	0.008	3.2×10^{-4}	1	0.008	3.2×10^{-4}	22
graphidiye-PVDF	0.033	6.6×10^{-3}	2.5	0.0132	2.64×10^{-3}	23
CNF-PVDF	0.0055	4.29×10^{-3}	4	1.375×10^{-3}	1.07×10^{-3}	24
CNT-Nafion	0.546	0.0546	4	0.1365	0.01365	25
PPy	0.1179	4.716×10^{-3}	1	0.1179	4.716×10^{-3}	26
PPy-TiO$_2$	0.0546	4.04×10^{-3}	0.6	0.091	6.73×10^{-3}	27
gel	0.403	6.72×10^{-4}	1	0.403	6.72×10^{-4}	28
gel-PI	0.23	1.898×10^{-3}	1.3	0.177	1.46×10^{-3}	29
Nanosheet MoS$_2$-Kapton	0.12	2×10^{-3}	0.3	0.4	6.6×10^{-3}	9
This work	0.244	0.015	1	0.244	0.015	

Furthermore, voltage-independent performance and voltage-dependent performance of these EAs are respectively shown in Fig. S7a,b.
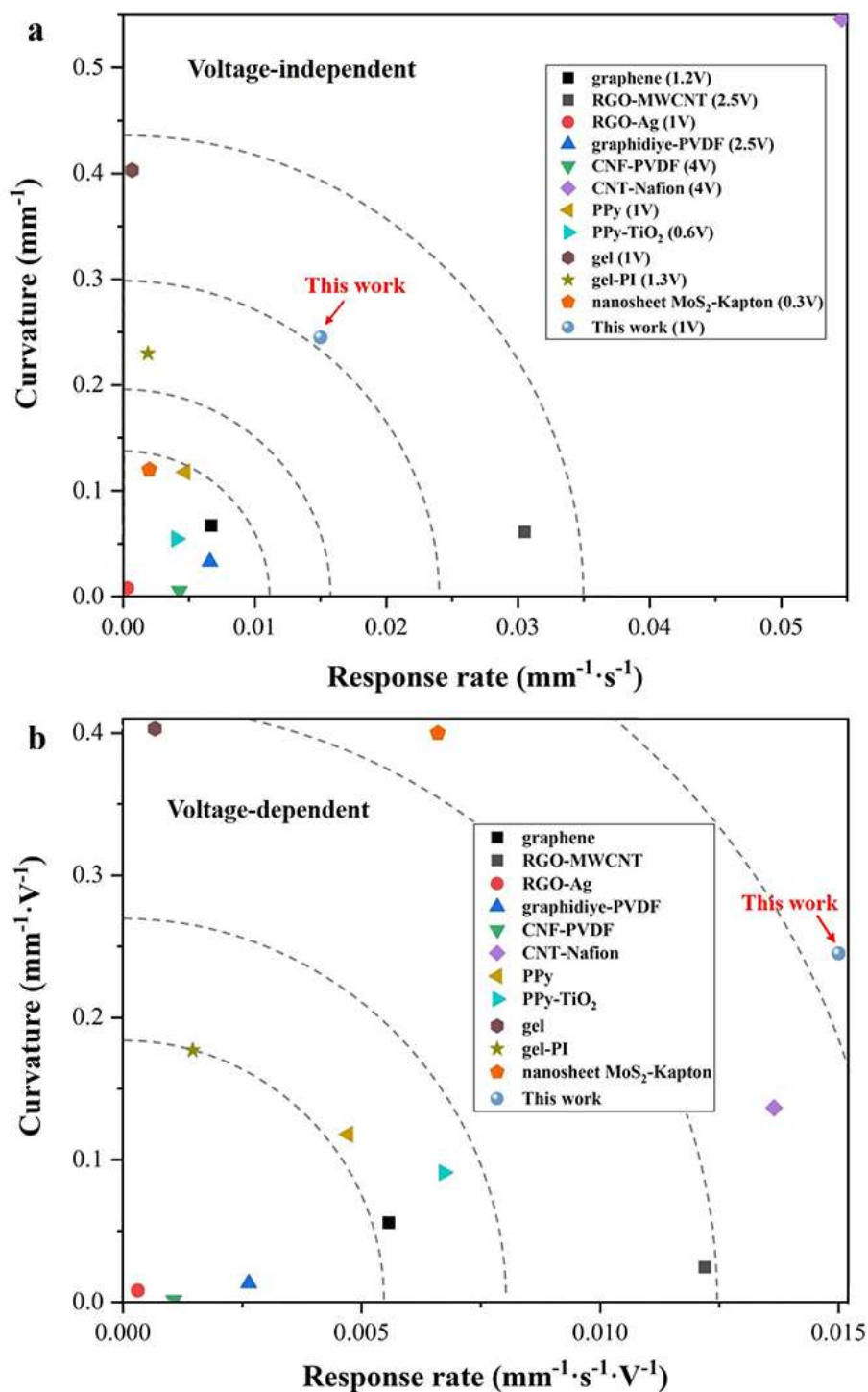
Fig. S7 (a) Voltage-independent and (b) voltage-dependent performance of existing EAs.

Section S8. Nanoindentation continuous stiffness measurement

Considering the thickness of the test film, the sample was prepared as following processes in order to ensure its uniformity. Firstly, a slide was cemented to an aluminum cylinder by using 120℃ hot melt adhesive, thereupon natural cooling took over until it reached room temperature,

then evenly-mixed A/B glue was coated on this slide. The test film was slightly put on the glue-coated slide, then we slightly compacted it by using another slide. Nanoindentation continuous stiffness measurement was performed after waiting for 4h in order to ensure the glue was dried off and fixed. The diamond Berkovich indenter was used in this measurement. Eight different positions on the prepared film were chosen for the measurement. It should be noted that, in order to avoid the influence of residual stress, the distance between indentations should be 30 times larger than the maximum indentation displacement.

Young's modulus and nanoindentation hardness of the chosen positions are shown in Fig. S8a,b, respectively. Both Young's modulus and nanoindentation hardness are larger at the surface of thin film, then they gradually decrease and become stable as the displacement increases. This is mainly caused by the surface effect of thin film.[30] Fig. S8c shows that the average Young's modulus and nanoindentation hardness of the 4μm MoS_2 film are $4.71 \pm 0.74 GPa$ and $0.27 \pm 0.06 GPa$, respectively. The deviations of Young's modulus and nanoindentation hardness at film surface are larger than the deviations at the interior region, which is caused by the effects of surface roughness. Moreover, a comparative measurement of fused silica was carried out to ensure the accuracy and reliability of measurement. In Fig. S8d, the average Young's modulus and nanoindentation hardness of fused silica are respectively found to be $71.08 \pm 0.61 GPa$ and $9.764 \pm 0.163 GPa$, which agree well with other's work.[31]
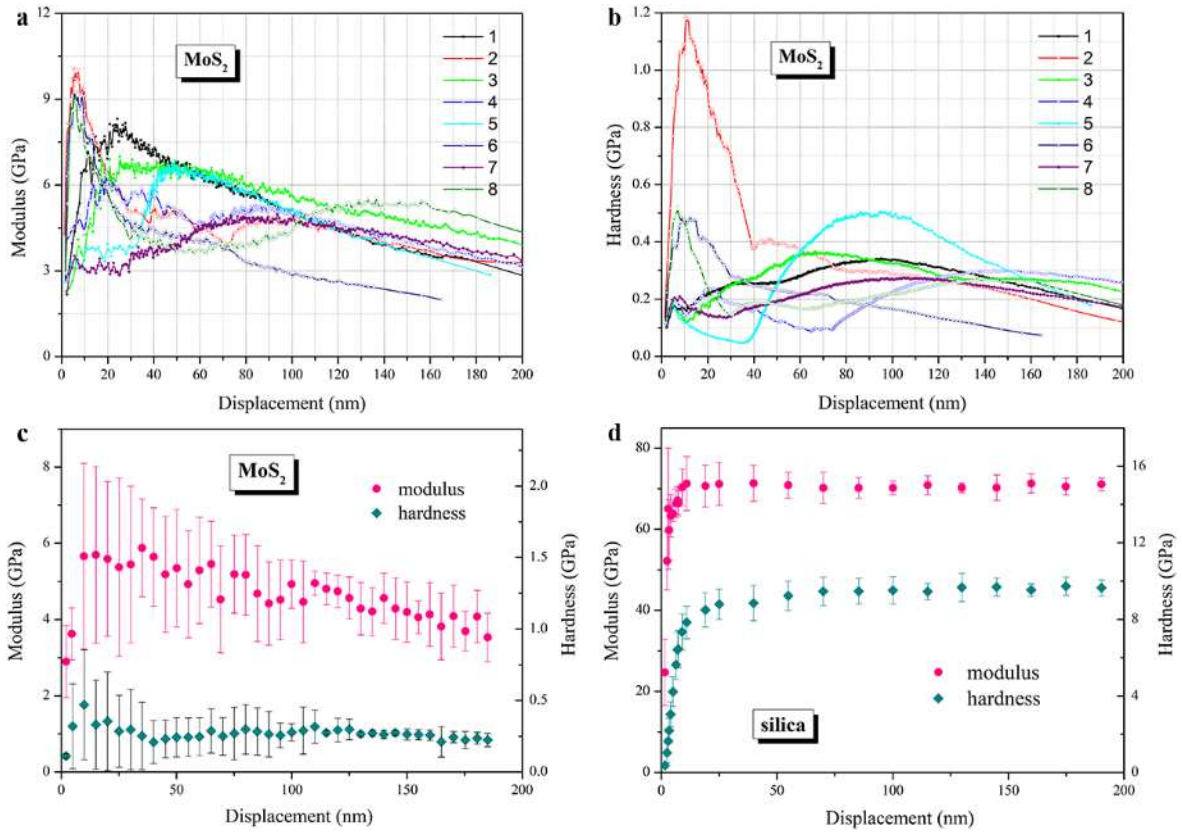
Fig. S8 (a) Young's modulus and (b) nanoindentation hardness at different positions of the 4μm MoS$_2$ film, numbers in the legends of (a) and (b) represent different positions. The average Young's modulus and nanoindentation hardness of (c) MoS$_2$ film and (d) fused silica.
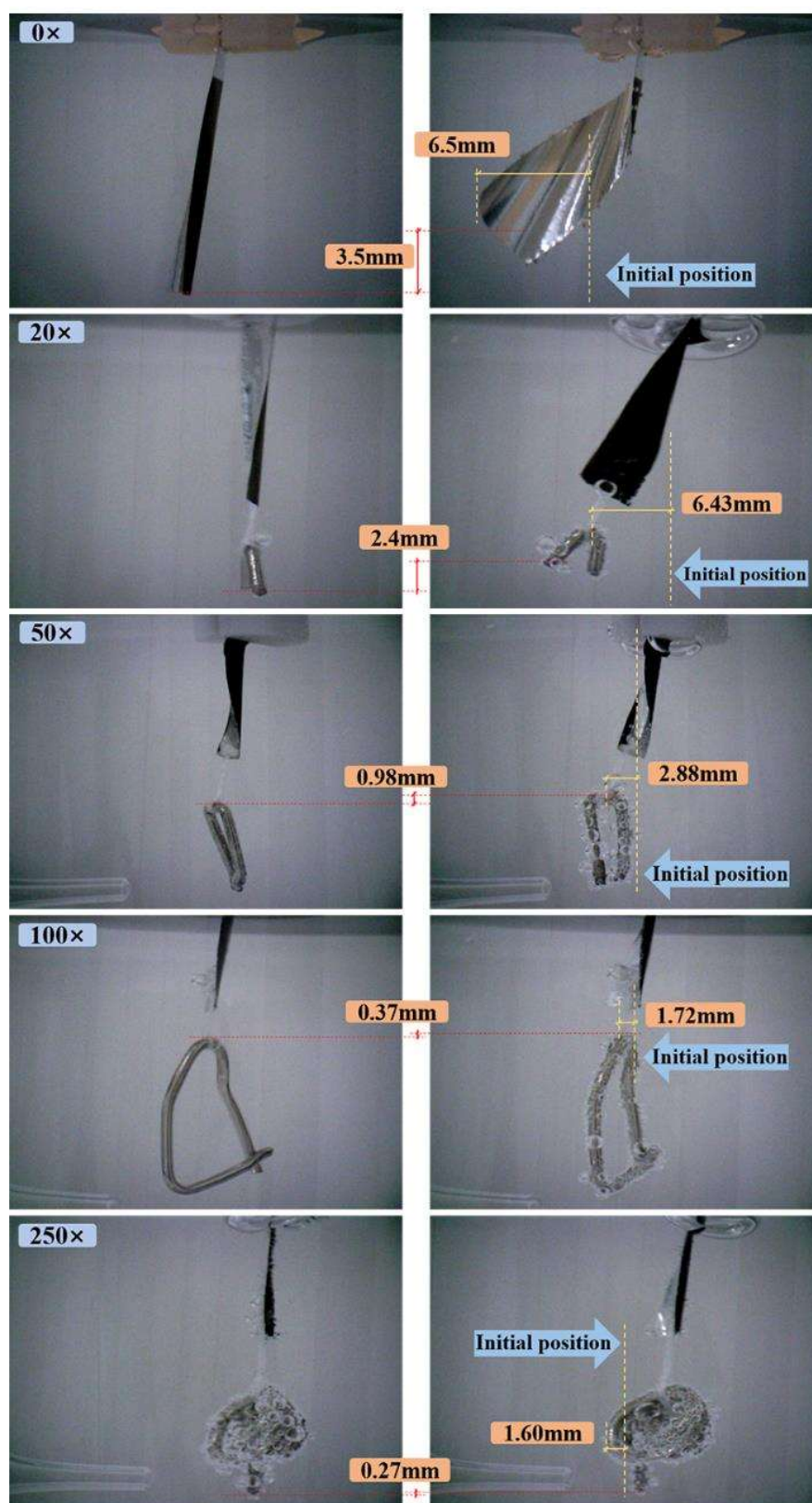
Section S9. Loading performance

Fig. S9 Loading performance of the EA under ±0.7V square wave potential. The numbers before multiplication represent the mass ratios of weight to actuator (MoS$_2$: 13mm×3mm×4μm; Al foil: 15mm×3mm×6μm).

References

[1] T. Komatsu and W. K. Hall, *J. Phys. Chem.,* 1992, **96**, 8131-8137.

[2] L. Ji, Z. Guo, S. Du and L. Chen, *Int. J. Mech. Sci.,* 2017, **134**, 599-609.

[3] X. Li, D. Xiao, H. Zheng, X. Wei, X. Wang, L. Gu, Y. S. Hu, T. Yang and Q. Chen, *Nano Energy,* 2016, **20**, 194-201.

[4] X. Zhang, W. Shyy and A. M. Sastry, *J. Electrochem. Soc.,* 2007, **154**, A910-A916.

[5] W. Shi, Y. Guo, Z. Zhang and W. Guo, *J. Phys. Chem. Lett.,* 2018, **9**, 6841-6846.

[6] Y. Huang, L. Liu, J. Sha and Y. Chen, *Appl. Phys. Lett.,* 2011, **110**, 104106.

[7] L. Shu, X. Wei, T. Pang, X. Yao and C. Wang, *Appl. Phys. Lett.,* 2017, **111**, 063902.

[8] P. S. Bass, L. Zhang, M. Tu and Z. Y. Cheng, *Actuators,* 2018, **7**, 72.

[9] M. Acerce, E. K. Akdoğan and M. Chhowalla, *Nature,* 2017, **549**, 370-373.

[10] L. Ji, Z. Guo and Y. Zhang, *Sci. China Technol. Sc.,* 2019, **62**, 1331-1340.

[11] J. Crank, *The Mathematics of Diffusion*, Oxford University Press, London, 1975.

[12] J. Pei, L. Huang, H. Jiang, H. Liu, X. Liu and X. Hu, *Sep. Purif. Technol.,* 2019, **210**, 651-658.

[13] L. Jiao, Y. Wang, Y. Zhi, W. Cui, Z. Chen, X. Zhang, W. Jie and Z. Wu, *Adv. Cond. Matter. Phys.,* 2018, **2018**, 1-5.

[14] Y. T. Ho, C. H. Ma, T. T. Luong, L. L. Wei, T. C. Yen, W. T. Hsu, W. H. Chang, Y. C. Chu, Y. Y. Tu, K. P. Pande and E. Y. Chang, *Phys. Status Solidi RRL,* 2015, **9**, 187-191.

[15] E. S. Hung and S. D. Senturia, *J. Microelectromech. S.,* 1999, **8**, 497-505.

[16] Y. J. Yang and H. H. Liao, *J. Micromech. Microeng.,* 2009, **19**, 025003.

[17] P. Eyabi and G. Washington, *Mechatronics,* 2006, **16**, 159-175.

[18] E. F. Crawley and J. de Luis, *AIAA J.*, 1987, **25**, 1373-1382.

[19] Q. Shi, C. Hou, H. Wang, Q. Zhang and Y. Li, *Chem. Commun.,* 2016, **52**, 5815-5819.

[20] X. Xie, L. Qu, C. Zhou, Y. Li, J. Zhu, H. Bai, G. Shi and L. Dai, *ACS Nano,* 2010, **4**, 6050-6054.

[21] G. Wu, G. H. Li, T. Lan, Y. Hu, Q. W. Li, T. Zhang and W. Chen, *J. Mater. Chem. A,* 2014, **2**, 16836.

[22] L. Lu, J. Liu, Y. Hu, Y. Zhang and W. Chen, *Adv. Mater.,* 2013, **25**, 1270-1274.

[23] C. Lu, Y. Yang, J. Wang, R. Fu, X. Zhao, L. Zhao, Y. Ming, Y. Hu, H. Lin, X. Tao, Y. Li and W. Chen, *Nat. Commun.,* 2018, **9**, 752.

[24] J. M. Park, S. J. Kim, J. H. Jang, Z. Wang, P. G. Kim, D. J. Yoon, J. Kim, G. Hansen and K. L. DeVries, *Compos. Part B-Eng.,* 2008, **39**, 1161-1169.

[25] S. Liu, Y. Liu, H. Cebeci, R. G. de Villoria, J. H. Lin, B. L. Wardle and Q. M. Zhang, *Adv. Funct. Mater.,* 2010, **20**, 3266-3271.

[26] G. Han and G. Shi, *Sensor Actuat. B-Chem.,* 2006, **113**, 259-264.

[27] X. He and G. Shi, *Sensor Actuat. B-Chem.,* 2006, **115**, 488-493.

[28] K. Takada, T. Iida, Y. Kawanishi, T. Yasui and A. Yuchi, *Sensor Actuat. B-Chem.,* 2011, **160**, 1586-1592.

[29] N. Hisamatsu, T. Iida, T. Yasui, K. Takada and A. Yuchi, *Sensor Actuat. B-Chem.,* 2014, **203**, 289-295.

[30] C. Walter, T. Antretter, R. Daniel and C. Mitterer, *Surf. Coat. Tech.,* 2007, **202**, 1103-1107.

[31] F. Dahmani, J. C. Lambropoulos, A. W. Schmid, S. J. Burns and C. Pratt, *J. Mater. Sci.,* 1998, **33**, 4677-4685.